Journal of Solid State Chemistry 182 (2009) 2004–2009

Contents lists available at ScienceDirect

Journal of Solid State Chemistry

journal homepage: www.elsevier.com/locate/jssc

Synthesis, crystal structure and characterization of iron pyroborate ($Fe_2B_2O_5$) single crystals

Tetsuya Kawano, Haruhiko Morito, Takahiro Yamada, Takeyoshi Onuma, Shigefusa F. Chichibu, Hisanori Yamane *

Institute of Multidisciplinary Research for Advanced Materials, Tohoku University, 2-1-1 Katahira, Aoba-ku, Sendai 980-8577, Japan

ARTICLE INFO

Article history:
Received 28 February 2009
Received in revised form
16 April 2009
Accepted 6 May 2009
Available online 14 May 2009

Keywords:
Iron pyroborate
Synthesis
Crystal structure
Single-crystal X-ray diffraction
Light transmittance
Diffuse reflectance
Cathodoluminescence
Magnetic susceptibility

ABSTRACT

Single crystals of iron(II) pyroborate, $Fe_2B_2O_5$, were prepared at 1000–1050 °C under an argon atmosphere. The crystals were transparent, yellowish in color and needle-like or columnar. The crystal structure of $Fe_2B_2O_5$ was analyzed by single-crystal X-ray diffraction. Refined triclinic unit cell parameters were $a = 3.2388(2)$, $b = 6.1684(5)$, $c = 9.3866(8)$ Å, $\alpha = 104.613(3)^\circ$, $\beta = 90.799(2)^\circ$ and $\gamma = 91.731(2)^\circ$. The final reliability factors of refinement were $R1 = 0.020$ and $wR2 = 0.059$ [$I > 2\sigma(I)$]. Transmittance over 50% in the visible light region from 500 to 750 nm was observed for a single crystal of $Fe_2B_2O_5$ with a thickness of about 0.3 mm. The light absorption edge estimated from a diffuse reflectance spectrum was at around 350 nm (3.6 eV). Magnetic susceptibility was measured for single crystals at 4–300 K. $Fe_2B_2O_5$ showed antiferromagnetic behavior below the Néel temperature, $T_N \approx 70$ K, and the Weiss temperature was $T_W = 36$ K. The effective magnetic moment of Fe was $5.3\mu_B$.

1. Introduction

In crystal structures of crystalline borates, BO_3 triangles and BO_4 tetrahedra can be connected with each other via common corners to form B_xO_y groups. The various crystal structures of borates are derived from the large diversity in the linkage of boron with oxygen [1,2]. The main-group metal borates have been studied as nonlinear optical crystals (β-BaB_2O_4, LiB_3O_5, $Sr_2Be_2B_2O_7$) and phosphors (SrB_4O_7, $BaLiB_5O_{10}$, $Ba_2Mg(BO_3)_2$) because of their transparency in a wide range from ultraviolet (UV) to infrared (IR) [3,4]. The magnetic and electrochemical properties of some transition metal borates such as MBO_3 (M = V, Cr, Fe) [5] and $M_3B_2O_6$ (M = Co, Ni, Cu) [6] have been studied.

In the Fe–B–O system, Fe(III) borates ($FeBO_3$ [7], Fe_3BO_6 [8]), Fe(II, III) borates (Fe_2BO_4 [9], Fe_3BO_5 [10]), and Fe(II) borates (α-FeB_2O_4 [11], FeB_4O_7 [12,13], $Fe_2B_2O_5$ [14]) have been studied. Fe(III) and Fe(II, III) borates are attracted due to their magnetic properties [15–18]. The physical properties of Fe(II) borates have not been reported, while a quartenary Fe(II) borate $LiFe^{2+}BO_3$ [19] was studied on its electrochemical properties as a cathode material with low cost and environmentally benign as well as $LiFe^{2+}PO_4$ [20] and $Li_2Fe^{2+}SiO_4$ [21].

$Fe_2B_2O_5$ has been synthesized by Block et al. with $Mg_2B_2O_5$ and $Mn_2B_2O_5$ [14]. They analyzed the crystal structure of $Mg_2B_2O_5$ and reported that $M_2B_2O_5$ (M = Mn, Fe) were isostructural with a triclinic phase of $Mg_2B_2O_5$ (2:2Δ type [1,2]) The unit cell parameters of $Fe_2B_2O_5$ were shown to be $a = 3.25$, $b = 6.18$, $c = 9.40$ Å, $\alpha = 104.17^\circ$, $\beta = 90.62^\circ$ and $\gamma = 91.48^\circ$, but the crystal structural parameters such as atomic coordinates, displacement parameters and so on were not presented in their paper, nor were details of $Fe_2B_2O_5$ single-crystal preparation. Magnesium pyroborate $Mg_2B_2O_5$, mineral name 'suanite', crystallizes in three crystallographic forms, a triclinic phase [14,22], a monoclinic phase [23] and a monoclinic phase with a doubled unit cell volume [24]. Triclinic pyroborates of other elements: $M_2B_2O_5$ (M = Mg [14,22], Mn [14,25,26], Fe [14], Co [14,27,28], Cd [29,30]), $MMnB_2O_5$ (M = Mg, Co) [31] and $M_{1.5}Zn_{0.5}B_2O_5$ (M = Co, Ni) [32] have also been reported. Fernandes et al. elaborated the crystal structure and magnetism of $Mn_2B_2O_5$ and $MgMnB_2O_5$ and showed antiferromagnetic behavior of $Mn_2B_2O_5$ with spin-flop-like transition [25]. Mn^{2+} doped $Cd_2B_2O_5$ is red phosphor utilized for fluorescent lamps [33].

In our preliminary study on borate compounds, we noticed that single crystals of $Fe_2B_2O_5$ are almost colorless and transparent, but optical and magnetic and properties of $Fe_2B_2O_5$ have not been investigated. In the present study, we synthesized single crystals of $Fe_2B_2O_5$ and analyzed the crystal structure by single-crystal X-ray diffraction (XRD). The optical and magnetic properties of $Fe_2B_2O_5$ were also characterized.

* Corresponding author. Fax: +81 22 217 5813.
E-mail address: yamane@tagen.tohoku.ac.jp (H. Yamane).

0022-4596/$ - see front matter © 2009 Elsevier Inc. All rights reserved.
doi:10.1016/j.jssc.2009.05.009

2. Experimental section

Starting powders of α-Fe (99.9%, Wako Pure Chemical Ind.), Fe_2O_3 (99.9%, Wako Pure Chemical Ind.) and B_2O_3 (99.99%, Kojundo Chemical Laboratory) were weighed with the predetermined molar ratios shown in Table 1. As-received B_2O_3 was stored and weighed in an argon-filled glove box due to its highly hygroscopic nature. The powders were mixed with approximately 5 ml of ethanol (99.5%, Wako Pure Chemical Ind.) in an agate mortar and pressed into pellets. The pellets were placed in a platinum (Pt) crucible and put into a quartz glass tube. The samples were heated at 1000–1050 °C for 3 h with a tubular furnace in an argon (99.9999%, Tokyo Koatsu Yamazaki) atmosphere. After heating, the samples were cooled to 900–950 °C at a cooling rate of 10 K h^{-1} and then cooled to room temperature by turning off the power of furnace.

The surface of the obtained single crystals was observed with a scanning electron microscope (SEM, Philips, ESEM XL-30) and elemental analysis of the crystals was carried out with an energy-dispersive X-ray (EDX) analyzer (EDAX, NEW XL-30) attached to the SEM.

The samples were powdered and characterized at room temperature by X-ray diffraction using Cu*K*α radiation with a graphite monochromator mounted on a powder diffractometer (Rigaku, RINT2000).

X-ray diffraction data of a single crystal were collected using Mo*K*α radiation with a graphite monochromator and an imaging plate on a single-crystal X-ray diffractometer (Rigaku, R-AXIS RAPID-II). Diffraction data collection and unit cell refinement were performed by the program PROCESS-AUTO [34]. Absorption correction was performed by the program NUMABS [35].

The crystal structure of $Fe_2B_2O_5$ was refined with the program SHELXL-97 [36] and WinGX software package [37] using the structural parameters of $Co_2B_2O_5$ reported by Rowsell et al. [28] as an initial structure model. Crystal structures were illustrated with the program VESTA [38].

Light transmittance of an $Fe_2B_2O_5$ single crystal 0.2–0.3 mm in thickness was measured with a color filter spectral inspection system (Otsuka Electronics, LCF-2100 M) in the region of 380–780 nm. Diffuse reflectance of the powdered sample was measured with a UV–Vis spectrophotometer (Hitachi, U-3000) and a 150 mm integrating sphere. Powdered $BaSO_4$ (Hitachi, white plate) was used as the reflectance standard from 200 to 900 nm. Cathodoluminescence (CL) measurement was carried out for a single crystal of $Fe_2B_2O_5$ at 12 and 300 K.

The temperature dependence of the magnetic susceptibility was measured using a Quantum Design SQUID magnetometer under zero field cooling (ZFC) conditions at an applied field of 10 kOe and 4–300 K.

3. Results and discussion

Table 1 lists the mixing molar ratios of the samples prepared in the present study and the obtained crystalline phases. All three starting mixtures melted by heating at 1000–1050 °C and single crystals of $Fe_2B_2O_5$ were formed at the bottom of the Pt crucible. The single crystals were transparent and yellowish, and had needle-like or columnar shapes. The crystals were easily cleaved along the plane perpendicular to their elongation direction. Fig. 1 shows an optical micrograph of a cleaved crystal with a thickness of 0.2–0.3 mm.

Table 1
Mixing molar ratios of the samples, heating temperatures and compounds in the Fe–B–O system.

Sample	Mixing molar ratio			Temperature (°C)	Compounds
	α-Fe	$\frac{1}{2}Fe_2O_3$	$\frac{1}{2}B_2O_3$		
A	45	0	55	1050	**$Fe_2B_2O_5$**, α-Fe, B_2O_3
B	2	4	6	1050	**$Fe_2B_2O_5$**, Fe_3BO_5
C	4	4	15	1000	**$Fe_2B_2O_5$**, B_2O_3

Sample A prepared with α-Fe and B_2O_3 consisted of $Fe_2B_2O_5$, α-Fe and B_2O_3, and contained a dispersion of fine α-Fe particles around 50 μm in size. These fine α-Fe particles could not be completely separated from $Fe_2B_2O_5$ crystal grains by magnetic separation and washing with acid solutions. Thus, Fe_2O_3 was added to the starting materials as a pro-oxidant for α-Fe in samples B and C.

$Fe_2B_2O_5$ would be formed by the following reaction:

$$2Fe + 2Fe_2O_3 + 3B_2O_3 = 3Fe_2B_2O_5$$

Yellow ($Fe_2B_2O_5$) and black (Fe_3BO_5) crystals were formed from the mixture with a molar ratio of Fe/B = 1.0 in the starting materials (sample B). Fe_3BO_5 was probably formed by evaporation of B_2O_3 during heating and the molar ratio Fe/B in the starting mixture became larger than 1.0. After the synthesis, an H_3BO_3 deposit, which was probably derived from the condensed B_2O_3, was observed in the cooler part of the quartz glass tube.

Excess B_2O_3 and α-Fe were added to the starting mixtures of sample C in order to maintain excess B_2O_3 and reduction conditions, since Fe_3BO_5 ($Fe_2^{2+}Fe^{3+}O_2BO_3$) includes Fe(III) ions. Most XRD peaks from the powdered sample C were indexed with the triclinic unit cell parameters of $Fe_3B_2O_5$. Preferred orientations of the $(\bar{1}02)$ and $(01\bar{1})$ planes were observed. Small XRD peaks of B_2O_3 were also seen, but no peaks from α-Fe and Fe_3BO_5 were detected.

SEM observation and EDX analysis of $Fe_2B_2O_5$ single crystals were performed without any conductive coating at an electron accelerating voltage of 10–20 kV. Only oxygen and iron elements were detected by EDX spectroscopy.

The crystal data and results of structure refinement for $Fe_2B_2O_5$ are summarized in Table 2. $Fe_2B_2O_5$ crystallizes in a triclinic unit cell ($P\bar{1}$ (No. 2)) and was refined with good final *R*-indices of $R1 = 0.020$ and $wR2 = 0.059$ [$I > 2\sigma(I)$]. Refined unit cell parameters ($a = 3.2388(2)$, $b = 6.1684(5)$, $c = 9.3866(8)$ Å, $\alpha = 104.613(3)^\circ$, $\beta = 90.799(2)^\circ$ and $\gamma = 91.731(2)^\circ$) were consistent with those reported by Block et al. ($a = 3.25$, $b = 6.18$, $c = 9.40$ Å, $\alpha = 104.17^\circ$, $\beta = 90.62^\circ$ and $\gamma = 91.48^\circ$).

Table 3 lists the refined positional parameters, and equivalent isotropic displacement parameters. Fe and B atoms have two sites, and O atoms have five sites. All these sites are at general 2*i*

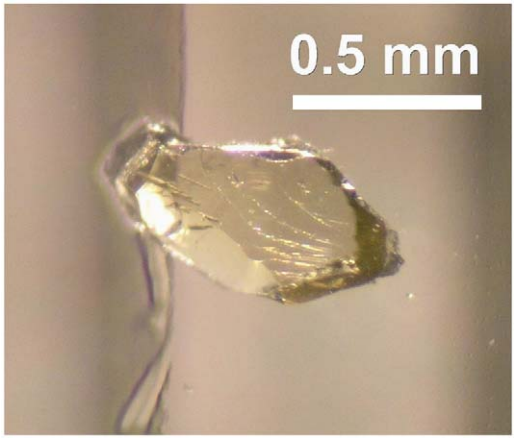

Fig. 1. Optical microscope photograph of a single crystal of $Fe_2B_2O_5$.

Table 2
Crystal data and structure refinement for $Fe_2B_2O_5$.

Chemical formula	$Fe_2B_2O_5$
Formula weight, M_r ($g\,mol^{-1}$)	213.32
Temperature, T (°C)	25(2)
Crystal system, space group	Triclinic, $P\bar{1}$ (No. 2)
Unit cell dimensions	$a = 3.2388(2)$ Å, $\alpha = 104.613(3)°$
	$b = 6.1684(5)$ Å, $\beta = 90.799(2)°$
	$c = 9.3866(8)$ Å, $\gamma = 91.731(2)°$
Unit cell volume, V (Å^3)	181.33(2)
Z	2
Calculated density, D_{cal}($Mg\,m^{-3}$)	3.907
Radiation wavelength (Mo$K\alpha$), λ (Å)	0.71073
Absorption coefficient, μ (mm^{-1})	7.89
F_{000}	204
Crystal size (mm^3)	$0.07 \times 0.06 \times 0.06$
2θ Range for data collection	6.8°–54.9°
Limiting indices	$-4 \le h \le 4$, $-8 \le k \le 8$, $-12 \le l \le 12$
Reflections collected/unique	1797/820 [$R_{int} = 0.023$]
Absorption correction	Numerical
Data/restraints/parameters	820/0/82
Goodness-of-fit on F^2, S	1.24
Final R indices [$I > 2\sigma(I)$]	
$R1$, $wR2$	0.020, 0.059
R indices (all data) $R1$, $wR2$	0.029, 0.042
Largest diff. peak and hole, $\Delta\rho$ ($e\,Å^{-3}$)	0.71 and −0.65

$R1 = \sum||F_o|-|F_c||/\sum|F_o|$. $wR2 = [\sum w \cdot (F_o^2 - F_c^2)^2 / \sum(w \cdot F_o^2)^2]^{1/2}$, $w = 1/[\sigma^2 \cdot (F_o^2) + (0.0118P)^2 + 0.2267P]$, where F_o is the observed structure factor, F_c is the calculated structure factor, σ is the standard deviation of F_c^2, and $P = (F_o^2 + 2F_c^2)/3$. $S = [\sum w \cdot (F_o^2 - F_c^2)^2/(n-p)]^{1/2}$, where n is the number of reflections and p is the total number of parameters refined.

Table 3
Atomic coordinates and equivalent isotropic displacement parameter, U_{eq}(Å^2), for $Fe_2B_2O_5$.

Atom	x	y	z	U_{eq}[a]
Fe1	0.73942(16)	0.20967(9)	0.36226(6)	0.00878(15)
Fe2	0.23610(16)	0.36376(9)	0.10085(6)	0.00766(15)
O1	0.2628(8)	0.6917(4)	0.0557(3)	0.0081(5)
O2	0.2224(8)	0.0870(5)	0.1813(3)	0.0111(5)
O3	0.7405(8)	0.4740(4)	0.2600(3)	0.0091(5)
O4	0.5545(8)	0.8568(4)	0.2980(3)	0.0120(6)
O5	0.7668(8)	0.7248(5)	0.5001(3)	0.0107(5)
B1	0.6986(12)	0.6782(7)	0.3539(4)	0.0073(8)
B2	0.3368(12)	0.8756(7)	0.1700(4)	0.0069(8)

All atoms are at 2*i* Wyckoff position with occupancy of 1.0.

[a] $U_{eq} = (\sum_i \sum_j U_{ij} a_i^* a_j^* \boldsymbol{a}_i \cdot \boldsymbol{a}_j)$.

Wyckoff position. Table 4 summarizes the bond lengths, bond angles, bond valence sums (BVSs) [39,40] and Baur's distortion indices [41] for $Fe_2B_2O_5$. The Fe–O distances (2.008(3)–2.336(3) Å) and B–O distances (1.343(5)–1.422(5) Å) almost agreed with those of other isostructural pyroborates mentioned above [14,22,26,28,30–32]. The BVSs of B at the triangular centers (B1: 3.00, B2: 2.98) and Fe at the octahedral sites (Fe1: 1.95, Fe2: 1.98) suggest that B and Fe are trivalent and divalent, respectively. Although both FeO_6 octahedra are distorted, the distortion index of $Fe1O_6$ (0.050) situated at the end of the ribbon is about two times larger than that of $Fe2O_6$ (0.021). The distortion indices of other isotypic pyroborates: $M_2B_2O_5$ (M = Mg [22], Mn [26], Co [28], Cd [30]) were 0.042–0.048 for $M1O6$ and 0.016–0.020 for $M2O_6$. The octahedra of substituted compounds ($MMnB_2O_5$ (M = Mg, Co) [31], $M_{1.5}Zn_{0.5}B_2O_5$ (M = Co, Ni) [32]) are largely distorted ($M1O_6$: 0.050–0.056, $M2O_6$: 0.020–0.025).

The coordination environments for Fe and B atoms are drawn with displacement ellipsoids in Fig. 2. B1 and B2 atoms are coordinated by three O atoms, and planar $B1O_3$ and $B2O_3$ triangles

Table 4
Selected bond lengths (Å), bond angles (°), bond valence sums (BVS), and distortion indices for $Fe_2B_2O_5$.

Bond length (Å)					
Fe1–O5^{i}	2.008(3)	Fe1–O5^{ii}	2.087(3)	Fe1–O3	2.091(3)
Fe1–O4^{iii}	2.170(3)	Fe1–O2^{iv}	2.324(3)	Fe1–O2	2.336(3)
Fe2–O2	2.033(3)	Fe2–O1^{v}	2.129(3)	Fe2–O1	2.169(3)
Fe2–O3	2.171(3)	Fe2–O1^{vi}	2.181(3)	Fe2–O3^{vii}	2.211(3)
B1–O5	1.343(5)	B1–O3	1.355(5)	B1–O4	1.422(5)
B2–O2^{viii}	1.345(5)	B2–O1	1.363(5)	B2–O4	1.416(5)
Fe1–Fe1^{iv}	3.2388(8)	Fe1–Fe2	3.2773(6)		
Fe2–Fe2^{iv}	3.2388(8)	Fe2–Fe2^{vi}	3.2945(6)	Fe2–Fe2^{v}	3.2293(6)
B1–B2	2.632(4)				
Bond angle (°)					
O3–B1–O5	124.7(4)	O3–B1–O4	119.2(3)	O4–B1–O5	116.2(3)
O1–B2–O2^{viii}	128.0(3)	O1–B2–O4	120.4(3)	O2^{viii}–B2–O4	111.6(3)
B1–O4–B2	136.0(3)				
Fe1–Fe2–Fe2^{iv}	60.28(4)	Fe2–Fe2^{iv}–Fe1	60.44(4)	Fe2^{iv}–Fe1–Fe2	59.28(4)
Fe2–Fe2^{iv}–Fe2^{vi}	61.24(4)	Fe2^{iv}–Fe2^{vi}–Fe2	59.52(4)	Fe2^{vi}–Fe2–Fe2^{iv}	59.24(4)
Bond valence sum[a]					
Fe1(VI)	1.95	Fe2(VI)	1.98		
B1(III)	3.00	B2(III)	2.98		
Distortion index[b]					
$Fe1O_6$	0.050	$Fe2O_6$	0.021		

Symmetry codes: (i) $-x+2$, $-y+1$, $-z+1$; (ii) $-x+1$, $-y+1$, $-z+1$; (iii) x, $y-1$, z; (iv) $x+1$, y, z; (v) $-x$, $-y+1$, $-z$; (vi) $-x+1$, $-y+1$, $-z$; (vii) $x-1$, y, z; (viii) x, $y+1$, z.

[a] Bond valence sum: $V_j \equiv \sum_i \exp[(l_0 - l_{ij})/B]$, where l_0 is the bond valence parameter (BVP) presented by Brese and O'Keefe for B–O and Fe–O, l_{ij} is the distance between i and j atoms, and B is a constant value of 0.37 Å. BVP values of B and Fe ions are $l_0(B^{3+}) = 1.371$ Å and $l_0(Fe^{2+}) = 1.734$ Å, respectively.

[b] Distortion index: $D \equiv 1/n \sum_i[(l_i - l_{av})/l_{av}]$, where l_i is the distance from the central atom to the nth coordinating atom, and l_{av} is the average bond lengths.

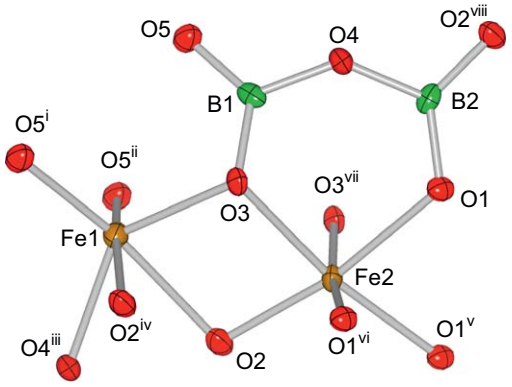

Fig. 2. Displacement ellipsoid plot of the iron and boron coordination environments within $Fe_2B_2O_5$ at 80% probability level. Symmetry labels correspond to those defined in Table 4.

are connected to form a B_2O_5 group by sharing with an O4 atom. Fe1 and Fe2 are in distorted oxygen octahedra.

As shown in Fig. 3(a), four FeO_6 octahedra are linked by edge-sharing to form an $[Fe_4O_{18}]$ unit. The $[Fe_4O_{18}]$ units are connected along the a-axis, and form a ribbon-like substructure, where four Fe atoms are arranged in the order of Fe1–Fe2–Fe2–Fe1 (Fig. 3(b)). The ribbons are parallel to the a-axis, and five O atoms of the B_2O_5 group belong to three adjacent ribbons. Therefore, $Fe_2B_2O_5$ has a quasi-one-dimensional structure. As shown by the dashed lines in Fig. 3(b), Fe atoms form a network which is almost hexagonal.

A light transmission spectrum for the single crystal of $Fe_2B_2O_5$ with a thickness of about 0.3 mm (Fig. 1) is shown in Fig. 4. The values of the transmittance were more than 40% in the region of 380–780 nm, which indicated that it has transparency in the visible light region. A diffuse reflection spectrum for the powdered sample is shown in Fig. 5. The values of reflectance of

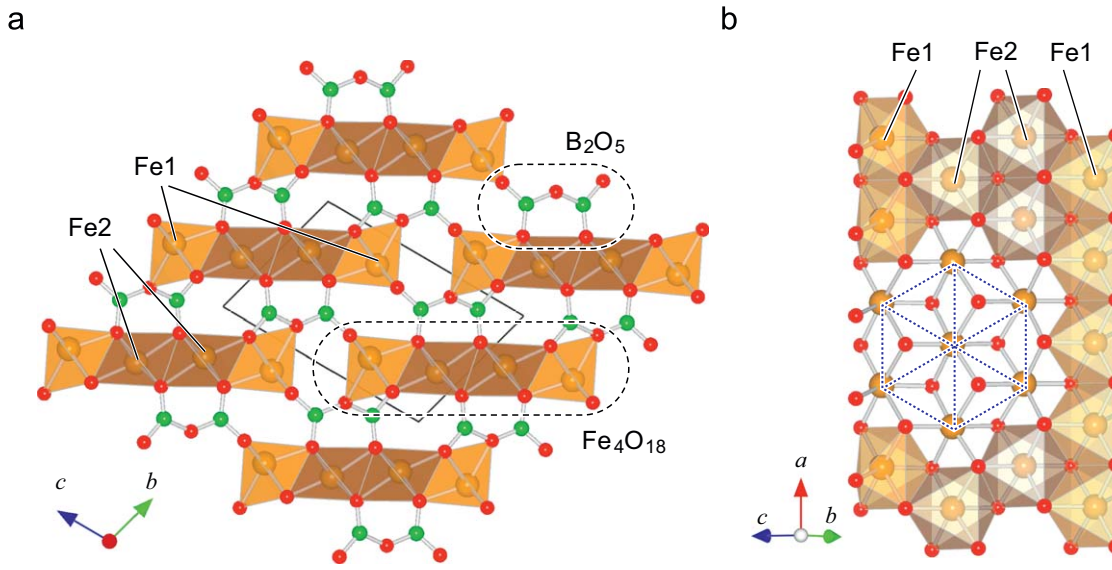

Fig. 3. (a) Crystal structure of $Fe_2B_2O_5$ viewed in the [100] direction using Fe-centered oxygen octahedra. Light and dark octahedra are $Fe1O_6$ and $Fe2O_6$, respectively. (b) View of a ribbon substructure drawn by using Fe-centered oxygen octahedra with an almost hexagonal arrangement of the Fe atoms.

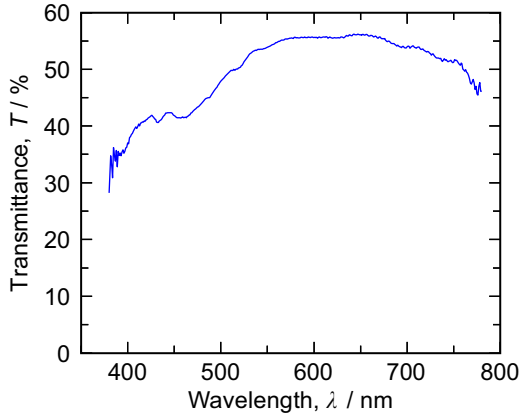

Fig. 4. Light transmission spectrum collected from the single crystal of $Fe_2B_2O_5$ shown in Fig. 1.

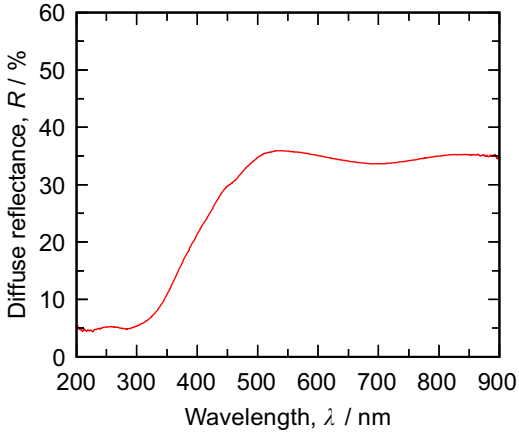

Fig. 5. Diffuse reflection spectrum of $Fe_2B_2O_5$ (R_{smp}).

$Fe_2B_2O_5$ (R_{smp}) were 35% in the region between 500 and 900 nm. The lights less than 500 nm in wavelength were absorbed, and the absorption edge was at 300 nm. The optical bandgap of $Fe_2B_2O_5$ estimated by analytical calculation using the Kubelka–Munk function [42,43] was around 3.6 eV.

The CL spectra of $Fe_2B_2O_5$ measured under excitation by an electron beam accelerated at 3.5 kV with 1.0×10^{-2} A cm^{-2} in current density are shown in Fig. 6. A broad peak of 3.3–5.1 eV and a strong peak of 5.799 eV were observed in the spectrum at 300 K. The broad emission peak would correspond to the optical bandgap of 3.6 eV estimated from the diffuse reflection spectrum. Strong, sharp peaks were observed at 5.505 and 5.594 eV in the spectrum measured at 12 K. Other small sharp peaks were detected at 3.321, 3.369 and 4.144 eV. Further investigations such as computational studies by using LDA+U and GGA+U methods would conduce to interpretation of the band gap and UV emission peaks based on an electronic structure of $Fe_2B_2O_5$.

Temperature dependence of the magnetic and inverse susceptibility shown in Fig. 7 indicates that $Fe_2B_2O_5$ is an antiferromagnet with a Néel temperature of $T_N\approx70$ K. A broad peak observed at around 70 K in the χ–T curve of $Fe_2B_2O_5$ probably indicates low-dimensional interactions derived from the ribbon-like substructures similar to those studied by Fernandes et al. for

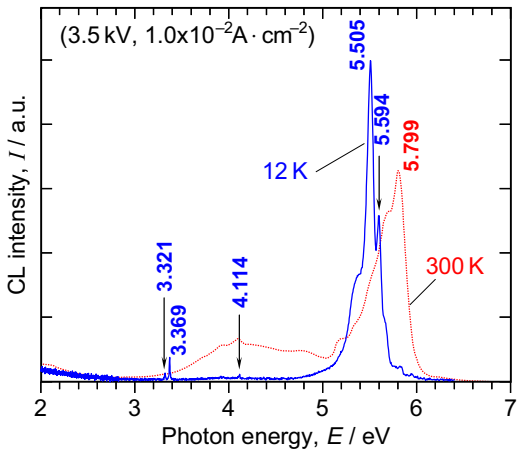

Fig. 6. Cathodoluminescence spectra of $Fe_2B_2O_5$ at 12 K (solid line) and 300 K (dotted line).

$Mn_2B_2O_5$ [25]. Sarrat et al. proposed spin configuration of $Mn_2B_2O_5$ based on the electron density distribution of $Mn_2B_2O_5$ by the maximum entropy analysis of single-crystal XRD data [26]. The distances between the Mn atoms of the adjacent ribbons are

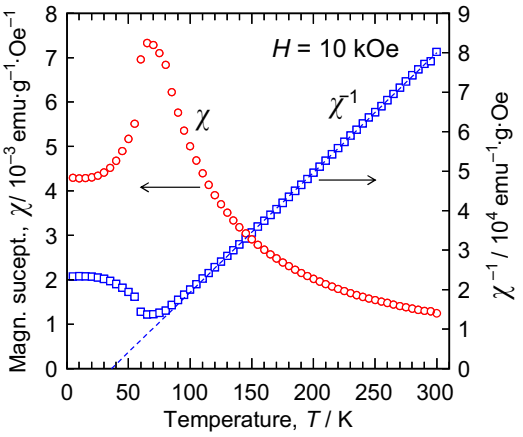

Fig. 7. Temperature dependence of the magnetic (circle) and inverse susceptibility (square) measured for $Fe_2B_2O_5$ in zero field cooling under an applied field of 10 kOe.

4.526–6.272 Å and electron density distributions were indicated in the regions between the ribbons. According to their model, all coplanar ribbons of $Mn_2B_2O_5$ were ferromagnetic, and antiferromagnetic behavior is derived from antiparallel magnetic orientation between adjacent ribbons. The distances from Fe1 to Fe1 and from Fe2 to Fe2 in the adjacent ribbons of $Fe_2B_2O_5$ are 4.3620(6) and 4.7867(7) Å, respectively. The Fe1–Fe2 and Fe2–Fe2 distances in the ribbon are 3.2587(5) and 3.2293(6)–3.2388(8) Å, respectively (Table 4). Therefore, intraplanar interactions of Fe atoms should be stronger than interplanar interactions.

The positive Weiss temperature $T_W = +36$ K suggested the existence of ferromagnetic spin–spin interactions. Antiferromagnetic $Mn_2B_2O_5$, which is a manganese analog of $Fe_2B_2O_5$, has a negative Weiss temperature of $T_W = -27.8$ K [25]. A similar relation has been reported for the ilmenites $M^{2+}TiO_3$ (M = Mn and Fe), having a layer magnetic structure. The Weiss temperatures of $FeTiO_3$ and $MnTiO_3$ were positive ($T_W = +59$ K) and negative ($T_W = -219$ K), respectively [44]. The intralayer ferromagnetic interactions of iron compounds are presumably higher than those of manganese compounds.

The Curie constant was $C = 3.517$ emu K mol-Fe^{-1} Oe^{-1} when the Curie–Weiss law was set at $\chi^{-1} = 2C/(T+T_W)$. The calculated effective magnetic moment of Fe, $P_{eff} = 5.3\mu_B$, well matches Stoner's empirical value ($5.25–5.53\mu_B$) [45], suggesting that Fe is divalent and in a high-spin state ($t_{2g}^4 e_g^2$) in $Fe_2B_2O_5$.

4. Conclusion

The crystal structure of Fe(II) pyroborate, $Fe_2B_2O_5$, with triclinic and space group $P\bar{1}$ (No. 2) was refined by single-crystal X-ray diffraction. The single crystals of $Fe_2B_2O_5$ were transparent with more than 40% transmittance in the visible light region of 380–780 nm. The optical bandgap estimated from the diffuse reflectance was 3.6 eV. Also, broad emission in the range from 3.3 to 5.1 eV and strong emission at around 5.8 eV were observed by cathodoluminescence spectroscopy. Temperature dependence of the magnetic susceptibility showed the Néel temperature of $Fe_2B_2O_5$ to be 70 K. The divalent and high-spin state of Fe in $Fe_2B_2O_5$ was shown by the effective magnetic moment of $5.3\mu_B$.

Supporting information

The crystallographic information file, a table of refined anisotropic displacement parameters (U_{ij}) and a list of structure factors of $Fe_2B_2O_5$ would be available as supplementary data at doi:10.1016/j.jssc.2009.05.009.

Acknowledgments

This work was supported in part by the Global COE Program "Materials Integration, Tohoku University", MEXT, Japan. The authors would like to thank Mr. Toshihiro Takada (Otsuka Electronics Co., Ltd., Japan) for the transmission measurement and Assoc. Prof. Asaya Fujita and Dr. Shun Fujieda (Tohoku University) for use of the SQUID equipment.

Appendix A. Supplementary material

Supplementary data associated with this article can be found in the online version at doi:10.1016/j.jssc.2009.05.009.

References

[1] P.C. Burns, J.D. Grice, F.C. Hawthorne, Can. Mineral. 33 (1995) 1131–1151.
[2] G. Heller, Top. Curr. Chem. 131 (1986) 39–98.
[3] P. Becker, Adv. Mater. 10 (1998) 979–992.
[4] D.A. Keszler, Curr. Opin. Solid State Mater. Sci. 4 (1999) 155–162.
[5] A.D. Balaev, N.V. Kazak, S.G. Ovchinnikov, V.V. Rudenko, L.V. Kirensky, N.B. Ivanova, Acta Phys. Pol. 34 (2003) 757–760.
[6] A. Débart, B. Revel, L. Dupont, L. Montagne, J.-B. Leriche, M. Touboul, J.-M. Tarascon, Chem. Mater. 15 (2003) 3683–3691.
[7] R. Diehl, Solid State Commun. 17 (1975) 743–745.
[8] R. Diehl, G. Brandt, Acta Cryst. B 31 (1975) 1662–1665.
[9] J.P. Attfield, J.F. Clarke, D.A. Perkins, Physica B 180–181 (1992) 581–584.
[10] J.S. Swinnea, H. Steinfink, Am. Mineral. 68 (1983) 827–832.
[11] J.S. Knyrima, H. Huppertz, J. Solid State Chem. 181 (2008) 2092–2098.
[12] T.A. Kravchuk, Y.D. Lazebnik, Russ. J. Inorg. Chem. 12 (1967) 21–24.
[13] I.M. Rumanova, E.A. Genkina, N.V. Belov, Izv. Akad. Nauk. Latv. SSR Ser. Khim. 5 (1981) 571–579.
[14] S. Block, G. Burley, A. Perloff, R.D. Mason Jr., J. Res. Natl. Bur. Stand. 62 (1959) 95–100.
[15] I.V. Pleshakov, V.V. Matveev, J. Phys. Condens. Matter 16 (2004) 1725–1731.
[16] C. Voigt, W. Roos, J. Phys. C Solid State Phys. 9 (1976) L469–L472.
[17] A.P. Douvalis, V. Papaefthymiou, A. Moukarika, T. Bakas, Hyperfine Interact 126 (2000) 319–327.
[18] M.A. Continentino, A.M. Pedreira, R.B. Guimarães, M. Mir, J.C. Fernandes, R.S. Freitas, L. Ghivelder, Phys. Rev. B 64 (2001) 014406-1–014406-6.
[19] Y.Z. Dong, Y.M. Zhao, Z.D. Shi, X.N. An, P. Fu, L. Chen, Electrochim. Acta 53 (2008) 2339–2345.
[20] A. Yamada, S.C. Chung, K. Hinokuma, J. Electrochem. Soc. 148 (2001) A224–A229.
[21] A. Nytén, A. Abouimrane, M. Armand, T. Gustafssona, J.O. Thomas, Electrochem. Commun. 7 (2005) 156–160.
[22] G.-C. Guo, W.-D. Cheng, J.-T. Chen, H.-H. Zhuang, J.-S. Huang, Q.-E. Zhang, Acta Cryst. C 51 (1995) 351–353.
[23] Y. Takéuchi, Acta Cryst. 5 (1952) 574–581.
[24] G.-C. Guo, W.-D. Cheng, J.-T. Chen, H.-H. Zhuang, J.-S. Huang, Q.-E. Zhang, Acta Cryst. C 51 (1995) 2469–2471.
[25] J.C. Fernandes, F.S. Sarrat, R.B. Guimarães, R.S. Freitas, M.A. Continentino, A.C. Doriguetto, Y.P. Mascarenhas, J. Ellena, E.E. Castellano, J.-L. Tholence, J. Dumas, L. Ghivelder, Phys. Rev. B 67 (2003) 104413-1–104413-7.
[26] F.S. Sarrat, R.B. Guimarães, M.A. Continentino, J.C. Fernandes, A.C. Doriguetto, J. Ellena, Phys. Rev. B 71 (2005) 224413-1–224413-6.
[27] S.V. Berger, Acta Chem. Scand. 4 (1950) 1054–1065.
[28] J.L.C. Rowsell, N.J. Taylor, L.F. Nazar, J. Solid State Chem. 174 (2003) 189–197.
[29] E.V. Sokolova, M.A. Simonov, N.V. Belov, Dokl. Akad. Nauk. SSSR 247 (1979) 603–606;
E.V. Sokolova, M.A. Simonov, N.V. Belov, Sov. Phys. Dokl. 24 (1979) 524–526.
[30] M. Weil, Acta Cryst. E 59 (2003) i95–i97.
[31] A. Utzolino, K. Bluhm, Z. Naturforsch. B 51 (1996) 912–916.
[32] S. Busche, K. Bluhm, Z. Naturforsch. B 50 (1995) 1445–1449.
[33] S. Kamiya, H. Mizuno, in: W. Yen, S. Shionoya, H. Yamamoto (Eds.), Phosphor Handbook, second ed., CRC Press, Boca Raton, FL, 2006, pp. 487–488.
[34] PROCESS-AUTO, Rigaku/MSC, 9009 New Trails Drive, The Woodlands, TX 77381-5209, USA, and Rigaku, 3-9-12 Akishima, Tokyo 196-8666, Japan. Rigaku/MSC & Rigaku Corporation, 2005.
[35] T. Higashi, NUMABS—Numerical Absorption Correction, Rigaku Corporation, Tokyo, 1999.
[36] G.M. Sheldrick, Acta Cryst. A 64 (2008) 112–122.
[37] L.J. Farrugia, J. Appl. Cryst. 32 (1999) 837–838.

[38] K. Momma, F. Izumi, J. Appl. Cryst. 41 (2008) 653–658.
[39] I.D. Brown, D. Altermat, Acta Cryst. B 41 (1985) 244–247.
[40] N.E. Brese, M. O'Keeffe, Acta Cryst. B 47 (1991) 192–197.
[41] W.H. Baur, Acta Cryst. B 30 (1974) 1195–1215.
[42] P. Kubelka, F. Munk, Z. Tech. Phys. 12 (1931) 593–601.
[43] S. Nara, S. Ibuki, in: W. Yen, S. Shionoya, H. Yamamoto (Eds.), Phosphor Handbook, second ed., CRC Press, Boca Raton, FL, 2006, pp. 28–32.
[44] J.J. Stickler, S. Kern, A. Wold, G.S. Heller, Phys. Rev. 164 (1967) 765–767.
[45] E.C. Stoner, Magnetism and Matter, Methuen, London, 1934, p. 312.